Article:

Gao, J., Knowles, A.J., Guan, D. orcid.org/0000-0002-3953-2878 et al. (1 more author) (2019) ω phase strengthened 1.2GPa metastable β titanium alloy with high ductility. Scripta Materialia, 162. pp. 77-81. ISSN 1359-6462

https://doi.org/10.1016/j.scriptamat.2018.10.043

ω phase strengthened 1.2GPa metastable β titanium alloy with high ductility

Junheng Gao[a]*, Alexander J Knowles[b], Dikai Guan[a], W. Mark Rainforth[a,]*

a Department of Materials Science and Engineering, The University of Sheffield, S1 3JD, UK

b Department of Materials, Royal School of Mines, Imperial College, London, SW7 2AZ, UK

*Corresponding author. E-mail address: junheng.gao@sheffield.ac.uk, m.rainforth@sheffield.ac.uk

Abstract

This paper provides a novel approach for exploiting ω phase strengthening in a metastable β titanium alloy whilst retaining high ductility. The addition of 1wt% Fe into our previously designed Ti-7Mo-3Cr alloy can efficiently control the growth of ω phase following air-cooling, resulting in a ultrahigh yield strength ($R_{p0.2}$of 1210 MPa) with large ductility (ε_f of 0.15). Transmission electron microscopy of the annealed Ti-7Mo-3Cr-1Fe alloy revealed that the air-cooled Ti-7Mo-3Cr-1Fe exhibited extensive ω precipitates 1-9nm in size, which were larger than that of its water-quenched counterpart (0.5-4 nm). EBSD and TEM results of deformed alloys showed that the growth of ω phase in the air-cooled Ti-7Mo-3Cr-1Fe alloy modified the deformation mechanism from {332} twinning and dislocation slip, in the water-quenched alloy, to localized dislocation plasticity in ω-void channels.

Keywords: Metastable beta titanium alloy; ω phase; Strengthening; Yield strength

Metastable β titanium alloys with twinning and/or martensite transformation induced plasticity (TWIP and/or TRIP) have been exploited as biomedical and structural materials owing to their low elastic modulus, low biotoxicity, high strength and large uniform elongation [1-5]. Recently, promising mechanical properties (e.g. high ductility and high hardening rate) have been achieved in metastable β titanium alloys, such as Ti-12Mo[6], Ti-9Mo-6W[7, 8], Ti-10Cr[9] and Ti-7Mo-3Cr[10], with TRIP and/or TWIP effects (hereafter all the compositions are in mass %). However, the low yield strength (200 -500MPa) of these metastable β titanium alloys with TRIP and/or TWIP has been their “Achilles’s heel”, hindering their technological application. Although some metastable titanium alloys with high yield strength have been observed, such as gum metal [11], these alloys generally show a low work hardening rate and poor uniform elongation.

Depending on the chemical compositions and cooling rate, after solid solution heat treatment in the high temperature β phase region[3], the martensite transformation and secondary phase precipitation (e.g. alpha phase and ω phase) can be activated separately or simultaneously, or the single-phase bcc structure retained. These different microstructures strongly influence the deformation mechanisms that occur upon loading. In the recent past, the influence of the ω phase on the strengthening effect in metastable β titanium alloys has been the subject of considerable interest. For example, Liu et al. developed a series of spinal-support metastable β titanium alloys with changeable modulus via deformation induced ω transformation [9, 12]. Moreover, Sun et al. [13] proposed that low-temperature flash aging of a Ti-12Mo alloy can effectively enhance the yield strength while preserving substantial elongation-to-failure, where the ω embrittlement effect was successfully avoided by the accurate temperature and time control for supressing of ω growth and elemental partitioning. Lai et al.[14] also studied the effect ω phase formation on the deformation mechanism of a metastable Ti-Nb-Ta-Zr alloy, and they reported that the formation of ω phase enhanced the yield strength and shifted the deformation mechanisms from $\{332\}$ twinning and martensite transformation, which were the main deformation mechanisms in the ω-free counterpart, to localized dislocation plasticity in ω-devoid channels.

In the current work, considering the formation of ω phase is also dependent on β phase stability (i.e. the amount of β stabilizers present) and cooling rate, we proposed a new route to exploit the ω phase strengthening effect while preserving high ductility. This led to a new metastable β titanium alloy, Ti-7Mo-3Cr-1Fe, optimised through β phase stability and cooling rate control. The Ti-7Mo-3Cr-1Fe alloy was developed based on our previously developed Ti-7Mo-3Cr alloy that had an initial deformation mechanisms of $\{332\}$ and as $\{112\}$ twinning and dislocation slip in water-quenched condition[10].

The Ti-7Mo-3Cr and Ti-7Mo-3Cr-1Fe alloys were arc melted from pure elements in a high-purity argon atmosphere. The ingots were homogenized at 1200℃ for 3h under flowing argon and water quenched. It was then cold rolled from 6 to 2.4mm thickness and annealed at 850℃ for 20 min under flowing argon, followed by water quenching or air cooling. X-ray diffraction was performed on a Siemens D5000 diffractometer fitted with a CuKα radiation source, at a scan rate of 0.1°/min and a step size of 0.01°. Tensile samples with a gauge dimension of 3mm×12.5mm×1.5mm were cut along the rolling direction and polished from the plate after heat treatment. Tensile tests were performed on a Zwick/Roell Z050 with laser extensometer at a strain rate of $4.0\times10^{-4}\ s^{-1}$. The anneaded and tensile tested plate samples with 2.4mm thickness were ground to ~100μm in thickness and punched to 3mm-diameter discs. Samples for EBSD imaging and TEM analysis were produced by twin-jet electropolished with a solution of 5% perchloric acid, 35% 2-butyoxyethanol and 60% methanol at -35℃. In order to obtain a relatively flat region at magnification of 500 × for EBSD mapping, the samples were electropolished for a short time (30-40 seconds) to remove the residual deformation surface layer induced by mechanical polishing. EBSD was performed using a field emission gun scanning electron microscope (FEI Inspect F50 FEG SEM) operated at 20kV with a step size of 1μm for grain size analysis and 0.15μm for twinning and phase analysis. A Tecnai T20 transmission electron microscope (TEM) operated at 200 kV was used to characterize the annealed and deformed samples. A double aberration corrected microscope JEM-Z3100F-R005 operated at 300 kV was also used to characterize the air-cooled Ti-7Mo-3Cr-1Fe alloy. A high-angle annular dark-field scanning transmission electron microscopy (HAADF-STEM) (JEOL 2100F) coupled with energy-dispersive spectroscopy (Oxford Instruments EDX detector) was used to investigate possible elemental partitioning with 0.7nm spot size and 15° tilt toward EDX detector.

After annealing at 850℃ for 20 min, a fully recrystallized microstructure with a broad grain size distribution (maximum 205μm, minimum 7μm) was observed for air-cooled Ti-7Mo-3Cr-1Fe alloy, Supplementary Figure 1, which corresponds well with the grain size distribution of Ti-7Mo-3Cr alloy[10]. The EBSD map indicated a single phase microstructure free from annealing twins and second phases for both air-cooled and water-quenched alloys.

Supplementary Figure 2 shows the XRD profiles of Ti-7Mo-3Cr-1Fe and Ti-7Mo-3Cr alloys subjected to air cooling or water quenching after annealing at 850℃ for 20 mins. For the water-quenched Ti-7Mo-3Cr-1Fe alloy, only peaks corresponding to β phase were identified, while both β phase and ω phase were observed in the air-cooled Ti-7Mo-3Cr-1Fe alloy, suggesting that the slower cooling rate induced more ω phase formation. For Ti-7Mo-3Cr alloy, β and ω phases were observed in the both air-cooled and water-quenched alloys. This suggests that both cooling conditions and the addition of 1% Fe can tailor the formation of ω phase.

Fig.1a shows a dark-field (DF) micrograph of the air-cooled alloy recorded using $(\bar{1}010)_{\omega 1}$, which shows the extensive formation of ω precipitates with a size in range of 1 to 9nm. The inset in Fig.1a presents the selected-area electron diffraction (SAED) pattern recorded along $[011]_{\beta}$ zone axis. Besides the distinct reflections from the β matrix, the pronounced diffraction intensity maxima at 1/3 and 2/3 $\{011\}_{\beta}$ positions provide further evidence of the extensive formation of ω precipitates. The DF image of the water-quenched alloy in Fig.1b also shows the extensive formation of ω precipitates, but the size of these precipitates was much smaller, 0.5 to 4nm, than that of air-cooled alloy. This was in agreement with the SAED pattern in the inset of Fig.1b, where the diffraction intensity maxima corresponding to ω phase were much weaker than that of ω phase in air-cooled alloy, suggesting that of amount of ω phase is smaller than that of air-cooled alloy. The DF micrographs of air-cooled and water-quenched Ti-7Mo-3Cr alloys are shown in Figs.1c and d. Insets in Figs.1c and d are their corresponding SAED patterns. In comparison with air-cooled and water-quenched Ti-7Mo-3Cr-1Fe alloys, the corresponding air-cooled and water-quenched Ti-7Mo-3Cr alloys exhibit larger ω precipitates, suggesting the addition of 1% Fe can tailor the ω precipitates size, instead of rapid growth of ω precipitates observed in air-cooled Ti-7Mo-3Cr alloy.

The ω phase in the air-cooled alloy was further characterized using HRTEM. Fig.2a shows the HRTEM image recorded along the $[\bar{1}10]_{\beta}$ zone axis, confirming the extensive formation of ω phase. Fig.2b shows the fast Fourier transform (FFT) pattern where both the β-associated and ω-associated spots are observed, which are consistent with the SAED pattern in Fig.1b. The inverse FFT image obtained by masking the ω spots (blue circles in Fig.2b) is shown in Fig.2c. Two ω variants are observed in the inverse FFT image, termed as $\omega_1$and ω_2. The size of $\omega_1$in the major and minor axis is 4.8nm and 4.1nm, respectively, while the size of $\omega_2$in the major and minor axis is 4.9nm and 3.8nm, which are consist with Fig.1a.

The STEM-HAADF image and corresponding EDX composition maps (Supplementary Figure 3) show no evidence of composition variation correlated with ω in the air-cooled Ti-7Mo-3Cr-1Fe alloy. The EDX maps show a uniform K-shell X-ray intensity for Ti, Mo, Cr and Fe over the entire mapping area, which is consist with the EDX composition maps of Ti-Nb alloy[15].

Fig.3 presents the tensile stress-strain curves of the Ti-7Mo-3Cr-1Fe alloy subjected to air-cooling or water-quenching after annealing at 850℃ for 20 min. For comparison, the stress-strain curves of air-cooled and water-quenched Ti-7Mo-3Cr alloys are also shown. The water-quenched Ti-7Mo-3Cr-1Fe exhibits a yield strength, $R_{p0.2}$ of 648MPa, ultimate tensile strength of 924MPa and strain to fracture of 0.25. Interestingly, air cooling substantially enhanced the yield strength ($R_{p0.2}$ of 1210MPa) and ultimate tensile strength (1245MPa) of the Ti-7Mo-3Cr-1Fe alloy, while retaining a large strain to fracture of 0.15. Although the Ti-7Mo-3Cr alloy exhibited high strength and high ductility in the water-quenched condition[10], the air-cooled Ti-7Mo-3Cr alloy fractured without observable plasticity.

Supplementary Figure 4a shows that neither martensite transformation nor twinning was observed in the air-cooled alloy at 3% tensile strain, although several band structures (marked by white arrows in Supplementary Figure 4a) were occasionally observed within some grains. For the water-quenched alloy (Supplementary Figure 4b), extensive $\{332\}\langle 113\rangle$ twins were observed, especially in relative large grains, where 2 or 3 twin variants activated. This corresponded well with our previous work in Ti-7Mo-3Cr alloy where the activation of twins was governed by both Schmid factor and grain size[10].

In order to determine the initial deformation mechanism, TEM analysis was conducted on the air-cooled Ti-7Mo-3Cr-1Fe after 3% total strain (Fig.4). The BF image in Fig.4a shows that a high density of nano-band structures are observed. According to the β[110] zone axis SAED pattern in Fig.4b, only β phase and ω phase are observed, indicating that these nano-band structures are not deformation twins or stress induced martensite. In order to identify these nano-band structures, DF images (Figs.4c and d) were obtained using ω reflections marked by ω_1 and ω_2 in Fig.4b. The DF images (Figs.4c and d) show that these nano-band structures are poor in ω phase, suggesting that these nano-band structures are ω-devoid dislocation channels, as reported in a furnace-cooled Ti-Nb alloy[14].

It is well accepted that the isothermal ω phase can cause embrittlement in metastable β titanium alloys. The growth of ω phase leads a rapid increase of local elastic strains around the interface between ω phase and β matrix, which act as obstacles for gliding dislocations[13]. The gliding dislocations are believed to cut through ω phase on the $\{112\}_{\beta}//\{\bar{1}100\}_{\omega}$ planes[14]. The growth of ω phase increases the critical resolved shear stress for dislocation motion, resulting in a high yield strength and loss of ductility (embrittlement). In order to exploit the strengthening effect of ω phase without significant loss of ductility, restricting the rapid ω phase growth is necessary.

The growth of ω phase in β titanium alloys is dependent on β stability (i.e. amount of β stabilizers) and cooling rate [1, 4, 14]. According to experimental knowledge and simulation work[1], Fe is one of the strongest β stabilizers among transition metals. The addition of Fe can greatly decreases the formation energy of β phase and meanwhile, Fe only has very limited effect on the formation energy of ω phase, so Fe is also one of the most efficient elements suppressing ω phase formation among the transition metals [1]. In the water-quenched Ti-Fe-Mo alloy [16, 17], very limited incommensurate ω phase (1nm domains) was observed. The different mechanical behaviour between the air-cooled Ti-7Mo-3Cr and Ti-7Mo-3Cr-1Fe alloys in Fig.3 and microstructural analysis in Figs.1 and 2 confirmed that the addition of 1wt% Fe successfully tailored the ω precipitates size in the air-cooled Ti-7Mo-3Cr-1Fe alloy, leading to a superior combination of high strength and high ductility.

Mantri et al. reported that, after annealing at 475 °C for 48h, the partitioning of Mo induced by the precipitation of ω phase in Ti-12Mo significantly stabilized the β matrix, resulting in a change of deformation mechanism from TWIP and TRIP to dislocation slip[18]. In this work, the change in the deformation mechanism in the air-cooled Ti-7Mo-3Cr-1Fe alloy was attributed to the growth of ω phase that acts as a strong barrier for $\{1\bar{1}0\}_\beta\langle 110\rangle_\beta$ atomic movements[14]. In metastable β titanium alloys, the shuffling of $\{1\bar{1}0\}_\beta$ planes along the $\langle 110\rangle_\beta$ direction is involved in the martensite transformation and twinning [14, 19]. In order to determine the effect of ω phase on the suppression of martensite transformation and twinning, Lai et al. calculated the shear modulus along $\{11\bar{2}0\}_\omega$ as this is parallel to $\{1\bar{1}0\}_\beta$ [14]. The shear modulus along $\{11\bar{2}0\}_\omega$ was calculated to be 39.55GPa, which was much larger than that of $\{1\bar{1}0\}_\beta$, <18GPa[14]. Therefore, it was the formation of a high density of larger ω precipitates in air-cooled Ti-7Mo-3Cr-1Fe alloy that acted as strong local barriers to $\{1\bar{1}0\}_\beta\langle 110\rangle_\beta$ atomic movements, which completely suppressed $\{332\}\langle 113\rangle$ twinning. As deformation twinning was completely suppressed in the air-cooled Ti-7Mo-3Cr-1Fe alloy, the plastic deformation of this alloy relied on localized dislocation slip in the nano-sized ω-devoid dislocation channels (Fig.4). The formation of the ω-devoid dislocation channels is attributed to the gliding of dislocations on the $\{112\}_\beta$ slip plane cutting though ω precipitates via the prismatic slip plane $\{\bar{1}100\}_\omega$ of the ω phase, which is parallel to the $\{112\}_\beta$ slip plane, and so promoted transformation of ω to β [20].

In summary, we report a new route to exploit the ω phase strengthening to obtain a superior combination of strength and ductility in a Ti-7Mo-3Cr-1Fe beta titanium alloy. The addition of 1wt% Fe in Ti-7Mo-3Cr alloy efficiently controlled the rapid growth of ω phase in the air-cooled condition, leading to an ultra-high yielding strength ($R_{p0.2}$ of 1210MPa) and large strain to failure (15%). We believe that much more substantial improvements can be achieved by further composition and cooling rate optimization.

Acknowledgements

This work is supported by the EPSRC project “Designing Alloys for Resource Efficiency (DARE)”, EP/L025213/1.

References

[1] L.F. Huang, B. Grabowski, J. Zhang, M.-J. Lai, C.C. Tasan, S. Sandlöbes, D. Raabe, J. Neugebauer, Acta Materialia, 113 (2016) 311-319.
[2] M. Niinomi, M. Nakai, J. Hieda, Acta Biomaterialia, 8 (2012) 3888-3903.
[3] M. Abdel-Hady, K. Hinoshita, M. Morinaga, Scripta Materialia, 55 (2006) 477-480.
[4] P. Wang, M. Todai, T. Nakano, Journal of Alloys and Compounds, 766 (2018) 511-516.
[5] P. Wang, Y. Feng, F. Liu, L. Wu, S. Guan, Materials Science and Engineering: C, 51 (2015) 148-152.
[6] F. Sun, J.Y. Zhang, M. Marteleur, T. Gloriant, P. Vermaut, D. Laillé, P. Castany, C. Curfs, P.J. Jacques, F. Prima, Acta Materialia, 61 (2013) 6406-6417.
[7] F. Sun, J.Y. Zhang, M. Marteleur, C. Brozek, E.F. Rauch, M. Veron, P. Vermaut, P.J. Jacques, F. Prima, Scripta Materialia, 94 (2015) 17-20.
[8] J. Gao, J. Nutter, X. Liu, D. Guan, Y. Huang, D. Dye, W.M. Rainforth, Scientific Reports, 8 (2018) 7512.
[9] H. Liu, M. Niinomi, M. Nakai, J. Hieda, K. Cho, Scripta Materialia, 82 (2014) 29-32.
[10] J. Gao, Y. Huang, D. Guan, A.J. Knowles, L. Ma, D. Dye, W.M. Rainforth, Acta Materialia, 152 (2018) 301-314.
[11] T. Saito, T. Furuta, J.-H. Hwang, S. Kuramoto, K. Nishino, N. Suzuki, R. Chen, A. Yamada, K. Ito, Y. Seno, T. Nonaka, H. Ikehata, N. Nagasako, C. Iwamoto, Y. Ikuhara, T. Sakuma, Science, 300 (2003) 464-467.
[12] H. Liu, M. Niinomi, M. Nakai, K. Cho, Acta Biomaterialia, 24 (2015) 361-369.
[13] F. Sun, J.Y. Zhang, P. Vermaut, D. Choudhuri, T. Alam, S.A. Mantri, P. Svec, T. Gloriant, P.J. Jacques, R. Banerjee, F. Prima, Materials Research Letters, 5 (2017) 547-553.
[14] M.J. Lai, T. Li, D. Raabe, Acta Materialia, 151 (2018) 67-77.
[15] E.L. Pang, E.J. Pickering, S.I. Baik, D.N. Seidman, N.G. Jones, Acta Materialia, 153 (2018) 62-70.
[16] A.J. Knowles, N.G. Jones, O.M.D.M. Messé, J.S. Barnard, C.N. Jones, H.J. Stone, International Journal of Refractory Metals and Hard Materials, 60 (2016) 160-168.
[17] A.J. Knowles, T.-S. Jun, A. Bhowmik, N.G. Jones, T.B. Britton, F. Giuliani, H.J. Stone, D. Dye, Scripta Materialia, 140 (2017) 71-75.
[18] S.A. Mantri, D. Choudhuri, T. Alam, V. Ageh, F. Sun, F. Prima, R. Banerjee, Scripta Materialia, 130 (2017) 69-73.
[19] H.Y. Kim, L. Wei, S. Kobayashi, M. Tahara, S. Miyazaki, Acta Materialia, 61 (2013) 4874-4886.
[20] M.J. Lai, C.C. Tasan, D. Raabe, Acta Materialia, 100 (2015) 290-300.

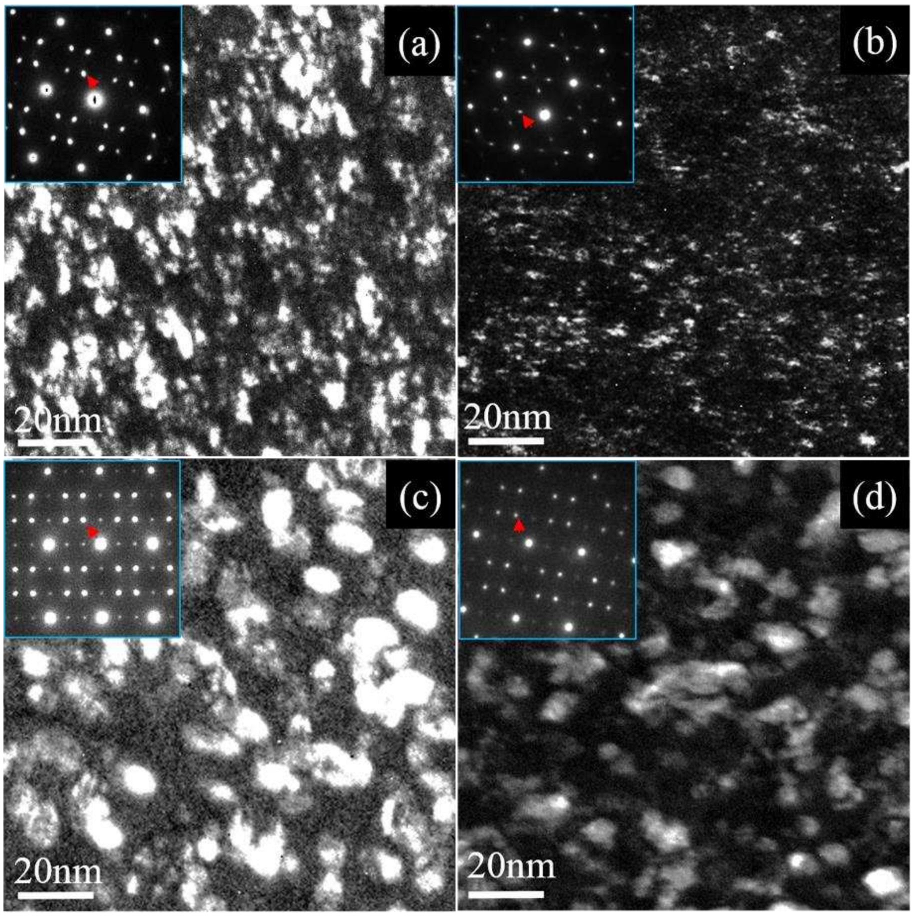

Fig. 1. TEM analysis of the annealed Ti-7Mo-3Cr-1Fe and Ti-7Mo-3Cr alloys subjected to air cooling or water quenching. (a) and (b) DF micrographs of Ti-7Mo-3Cr-1Fe alloy subjected to air cooling and water quenching respectively; (c) and (d) DF micrographs of Ti-7Mo-3Cr alloy subjected to air cooling and water quenching respectively. DF images were recorded using $(\bar{1}010)_{\omega 1}$, marked by red arrow in the SAED patterns (Insets). SAED patterns were recorded with beam//$[011]_{\beta}$.

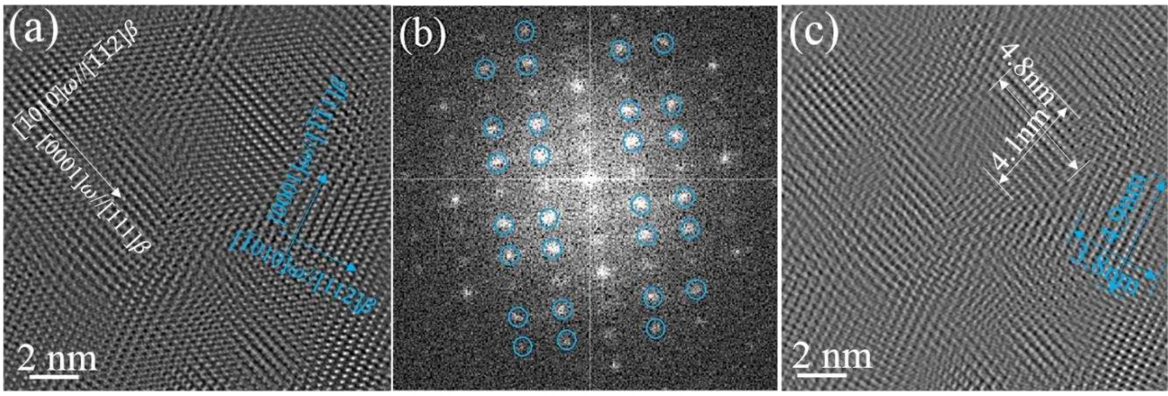

Fig.2.HRTEM study of the annealed Ti-7Mo-3Cr-1Fe alloy subjected to air cooling. (a) HRTEM image recorded along the $[\bar{1}10]_{\beta}$ zone axis,(b) corresponding FFT pattern, (c) inverse FFT image by masking the ω spots (blue circles) in (b).

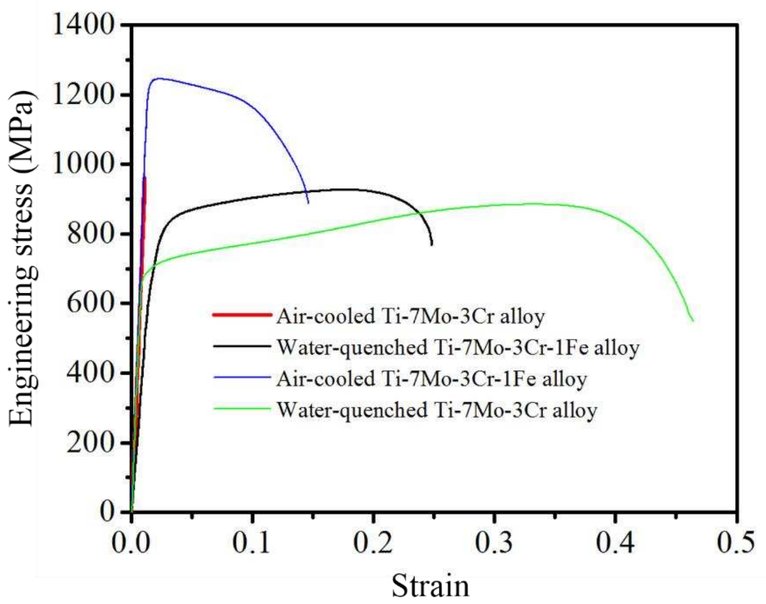

Fig.3. Tensile engineering stress-strain tensile curves of Ti-7Mo-3Cr and Ti-7Mo-3Cr-1Fe alloys subjected to air cooling or water quenching after annealing.

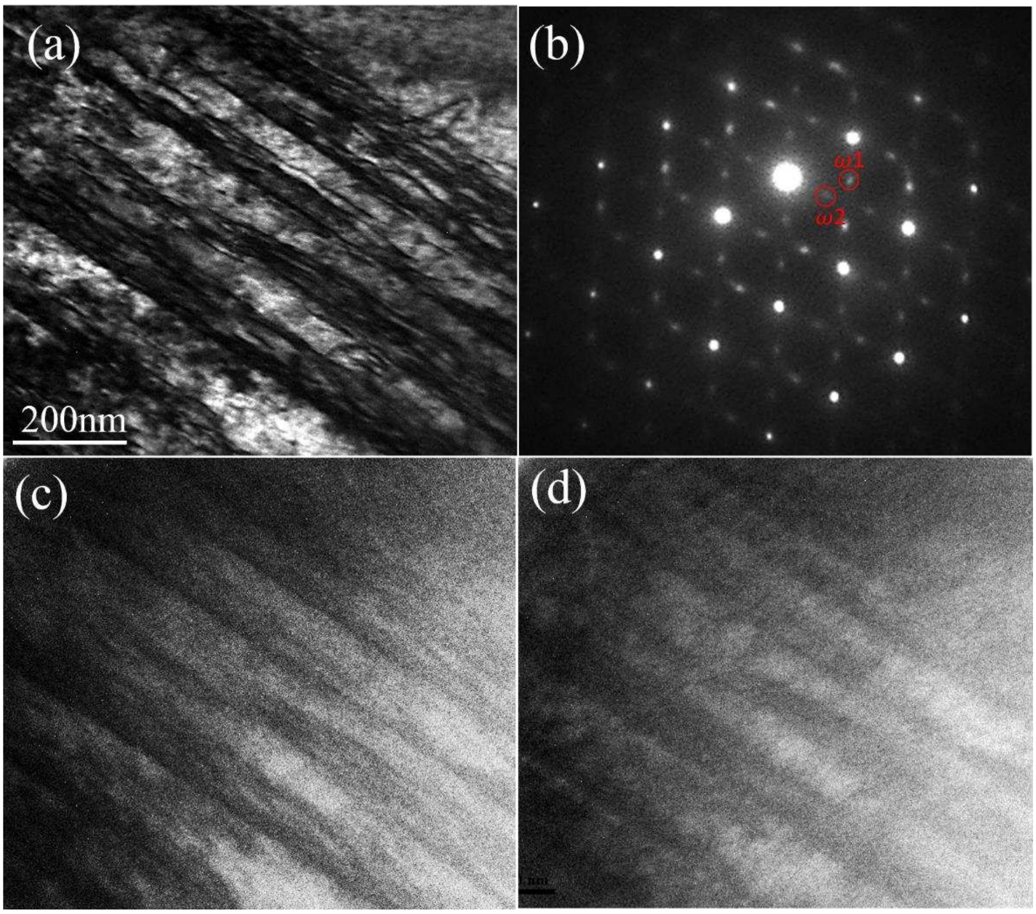

Fig.4. TEM analysis of the tensile-tested air-cooled Ti-7Mo-3Cr-1Fe alloy after 3% total strain. (a) BF image and its indexed β[110] zone axis SAED pattern (b). (c) and (d) corresponding DF images acquired using ω reflections marked by ω_1(c) and ω_2 (d) in (b).